RSC Advances

ROYAL SOCIETY OF CHEMISTRY

PAPER

View Article Online
View Journal | View Issue

Check for updates

Cite this: *RSC Adv.*, 2020, **10**, 34033

Quinazoline-Schiff base conjugates: *in silico* study and ADMET predictions as multi-target inhibitors of coronavirus (SARS-CoV-2) proteins

Mostafa A. Mansour,[a] Asmaa M. AboulMagd[a] and Hamdy M. Abdel-Rahman*[ab]

Received 23rd July 2020
Accepted 2nd September 2020

DOI: 10.1039/d0ra06424f

rsc.li/rsc-advances

The 2019 coronavirus (COVID-19) pandemic is spreading worldwide, with a dramatic increase in death without any effective therapeutic treatment available up to now. We previously reported quinazoline-trihydroxyphenyl Schiff base conjugates as phosphodiesterase 4B (PDE 4B) inhibitors (an enzyme that plays an essential role in the early stages of COVID-19 pneumonia). Additionally, the structural similarity between these conjugates and identified anti-severe acute respiratory syndrome (SARS)-coronavirus (CoV)-2 flavonoids inspired us to *in silico* study their possible binding interactions with essential SARS-CoV-2 proteins. Thus, this study provides an insight into the potential bindings between quinazoline-Schiff base conjugates and SARS-CoV-2 proteins, including spike glycoprotein (SGp), main protease (M^{pro}) and RNA-dependent RNA polymerase (RdRp), to offer an opportunity to find an effective therapy. Besides this, based on the role that COVID-19 plays in iron dysmetabolism, the conjugate trihydroxyphenyl moiety should be reconsidered as an iron chelator. Moreover, molecular dynamics simulations of quinazoline derivative **Ic** bound to the mentioned targets were carried out. Finally, ADMET calculations were performed for the studied compounds to predict their pharmacokinetic profiles.

1. Introduction

Since the emergence of severe acute respiratory syndrome (SARS) coronavirus (CoV) in Wuhan, China at the end of 2019, extensive studies on the pathogenicity and transmissibility of the causative virus, SARS-CoV-2, have been discussed.[1] COVID-19 is considered the seventh coronavirus known to infect humans and cause severe diseases.[2] Coronaviruses are enveloped structures, their RNA nucleic acid is positive and single-stranded, meaning that they can infect both humans and animals, especially cattle.[3] The virus releases a *S*-glycoprotein on its surface that is responsible for its attachment to a host receptor, named angiotensin-converting enzyme 2 (ACE2), during cell entry.[4] The sequencing of the SARS-CoV-2 genome revealed that it encodes for 16–17 non-structural proteins. Two proteases, namely papain-like protease (PLpro) and 3-chymotrypsin-like protease (3CLpro), which are known as M^{pro}, are essential in both maturation and infectivity of the virus.[5–10] Additionally, RNA-dependent RNA polymerase (RdRp) allows the viral genome to be copied into the new RNA strand using the host cell's machinery[11–15] (Fig. 1).

A recent literature survey highlighted that two possible viral pathophysiological mechanisms exist. The first one deals with interaction with the hemoglobin molecule, through receptors present on erythrocyte precursors, such as CD147 (also known as Basigin or EMMPRIN) or cluster of differentiation 26 (CD26), causing COVID-19. In contrast, the other mechanism is the induction of a ferroportin blockage through hepcidin-mimetic action of a viral spike protein.[16,17] Regarding iron dysmetabolism in SARS-CoV-2, a noticeable similarity between the hepcidin protein and SARS-CoV-2 spike glycoprotein cytoplasmic tail amino acid sequence has been reported.[18] SARS-CoV-2 has evolved to use a variety of host proteases, including cathepsin L, cathepsin B, trypsin, factor X, elastase, furin, and TMPRSS2

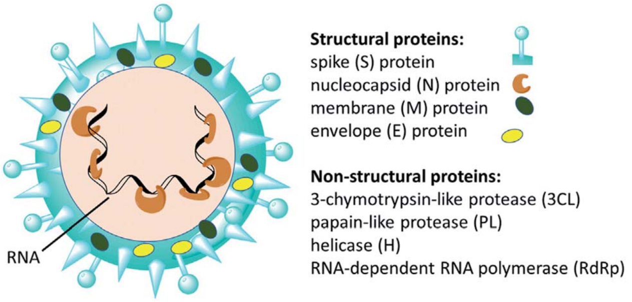

Fig. 1 Scheme of SARS-CoV-2 and some of its molecular protein targets.[6]

---

[a] *Pharmaceutical Chemistry Department, Faculty of Pharmacy, Nahda University (NUB), Beni-Suef, Egypt. E-mail: hamdy.abdelrahman@nub.edu.eg*

[b] *Medicinal Chemistry Department, Faculty of Pharmacy, Assiut University, Assiut 71526, Egypt*

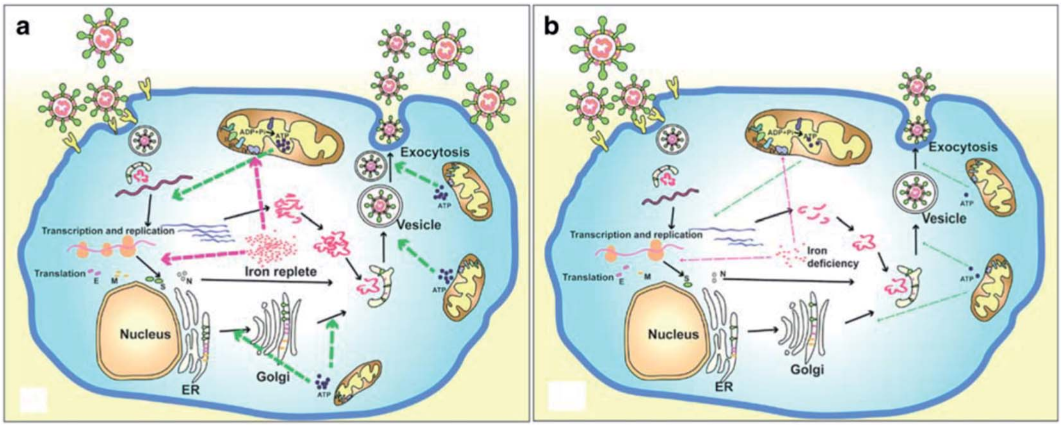

Fig. 2 Life cycle of coronaviruses under iron replete and deficiency conditions. (a) Sufficient intracellular iron levels support coronavirus replication, whereas (b) iron deficiency undermines its replication process by interfering with viral transcription, translation, assembly, and exocytosis. CoVs enter into host cells *via* binding to various receptors and disassemble to release the viral genome and nucleocapsid.[21]

(transmembrane protease serine 2), to facilitate cell entry following receptor binding. It has been revealed that circulating Ang II levels are markedly increased in COVID-19 patients, providing a direct connection between tissue ACE2 down regulation with SARS-CoV-2 *via* blocking of the receptor binding domain (RBD) of the viral S-protein.[19] Hepcidin is considered as the master regulator of iron metabolism, interacting with ferroportin to increase the iron entrance inside the cells.[20] In terms of COVID-19, significant iron metabolism dysregulation may occur, accompanied by hyperferritinemia and ultimately ferroptosis.[21] Whether the main pathological viral infection begins in the lungs, resulting in general anemic hypoxia or the opposite, iron dysmetabolism, is a matter of future research due to its role in multi-organ disease and hypoxia (Fig. 2).

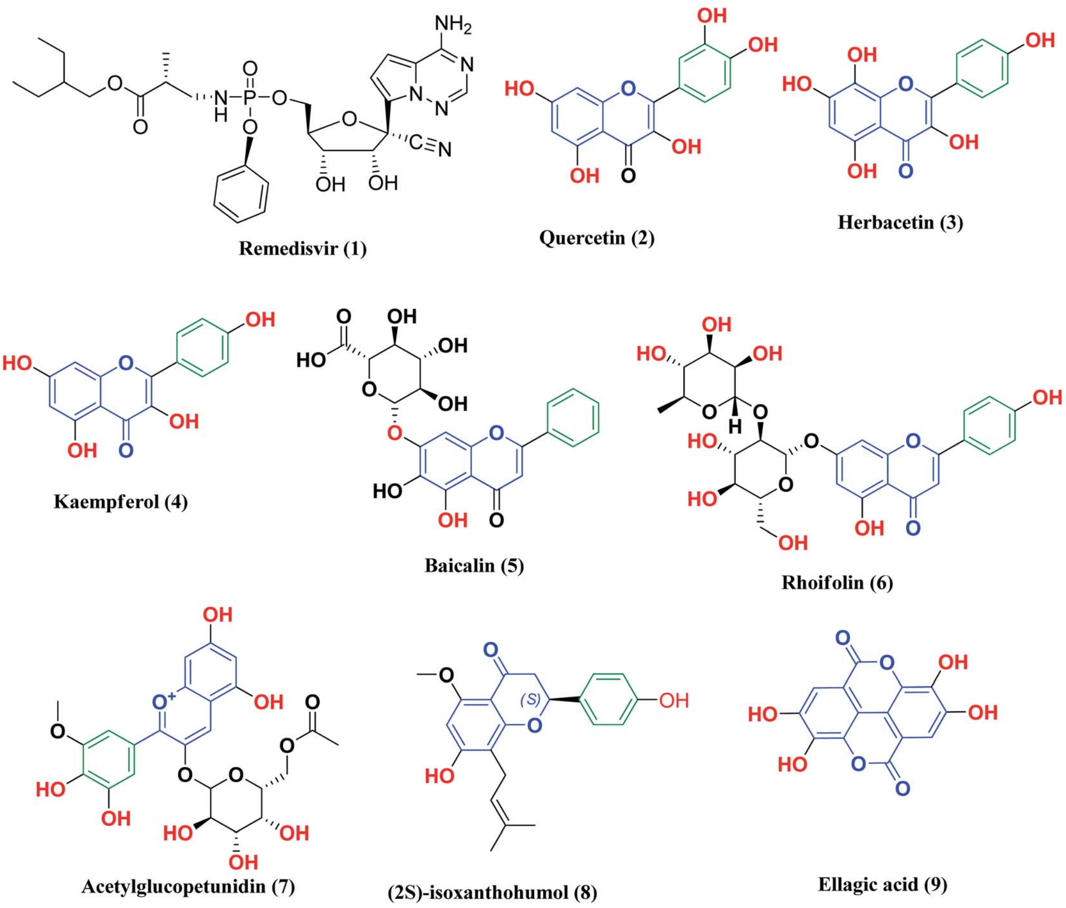

Fig. 3 Remdesivir and reported polyphenolic compounds that are possible SARS-CoV-2 3CLpro inhibitors.

Although the hallmarks of COVID-19 have been studied in detail, until now there has been no specific drug used in its treatment, with its control mainly being achieved using known antiviral drugs combined with supportive care.[22] Thus, many research groups worldwide began searching for drugs and/or molecules for rapid COVID-19 disease therapy from libraries of natural, synthetic or semi-synthetic derivatives. The main strategies for these drug discovery projects involve repurposing of approved drugs or using computational approaches such as molecular docking, virtual screening, simulations, *etc.*, which can save time, money and facilitate the discovery of COVID-19 drugs.[23]

Remdesivir **1** (Fig. 3) was the first drug granted emergency use for the treatment of suspected or laboratory confirmed COVID-19 cases by the U.S. Food and Drug Administration (FDA). It is an antiviral nucleoside analog that was developed for treatment of general ribonucleic acid (RNA) viral infections. It works by inhibiting viral replication through competitively inhibiting viral RNA polymerase.[24]

Other research projects have focused on adjuvant therapies for the treatment of COVID-19, in particular iron chelation and phosphodiesterase 4 (PDE 4B) inhibitors. As previously mentioned, COVID-19 infections are characterized by iron dysmetabolism resulting in increasing intracellular iron, thus depriving iron supply to the virus represents a promising adjuvant therapy. For this reason, iron chelators such as deferoxamine or polyphenols have been screened for their effectiveness against SARS-CoV-2 viral infection.[25] On the other hand, PDE4 inhibitors, which are one of the major PDE enzymes involved in cAMP-mediated regulation, play an important role in suppressing inflammatory cell functions that contribute to their anti-inflammatory actions in respiratory diseases such as chronic obstructive pulmonary disease (COPD) and asthma. Furthermore, the inhibition of PDE4 activity leads to smooth muscle relaxation and bronchodilation, which is useful for the treatment of asthma or COPD.[26–29] Thus, selective PDE 4B inhibitors may be a promising option for treatment of the COVID-19 early hyperinflammatory state attributed to massive pro-inflammatory cytokine release.[30]

Likewise, many polyphenolic natural products such as flavonoids (**2**–**6**) have been *in silico* screened as a possible therapeutic treatment for COVID-19 disease as 3CLpro inhibitors (Fig. 3).[31–33] In our previous study, three more phenolic compounds (**7**–**9**) were also screened against the SARS-CoV-2 main protease (M^{pro}) enzyme (Fig. 3). The structure–activity relationship analyses of the final top-hits presented in Fig. 3 reveal that they share similar binding modes in terms of hydrogen bonding and van der Waals interactions within the active site of M^{pro}.[34]

From all the above mentioned studies, we think that an effective protocol for the treatment of COVID-19 disease should include the following; (a) a drug that disrupts the life cycle of the virus at any stage of the viral replication cycle, such as blocking ACE2 receptors or inhibition of the SARS-CoV-2 main protease (M^{pro}); (b) an iron chelating agent to bind with the excess iron resulting from its dysmetabolism; (c) anti-inflammatory drugs as phosphodiesterase 4 inhibitors for the treatment of lung inflammation and necrosis.

We previously reported the design and synthesis of a class of 3*H*-quinazolin-4-one/Schiff base conjugates and evaluated them in terms of their PDE 4B activity.[35] Based on the above findings, as the most active derivatives of this series were trihydroxyphenyl Schiff bases, we thought that these compounds would be ideal drugs for the treatment of COVID-19 (Fig. 4). Thus, herein we perform molecular modeling studies on the quinazolinone-Schiff base conjugates against three essential target proteins of the SARS-CoV-2 virus and predict their pharmacokinetics properties for rapid drug discovery.

2. Experimental

2.1. Chemistry

The synthesis of the target substituted 2-phenylquinazoline derivatives was performed according to previously reported work.[35–37] Details of the synthetic procedures as well as full

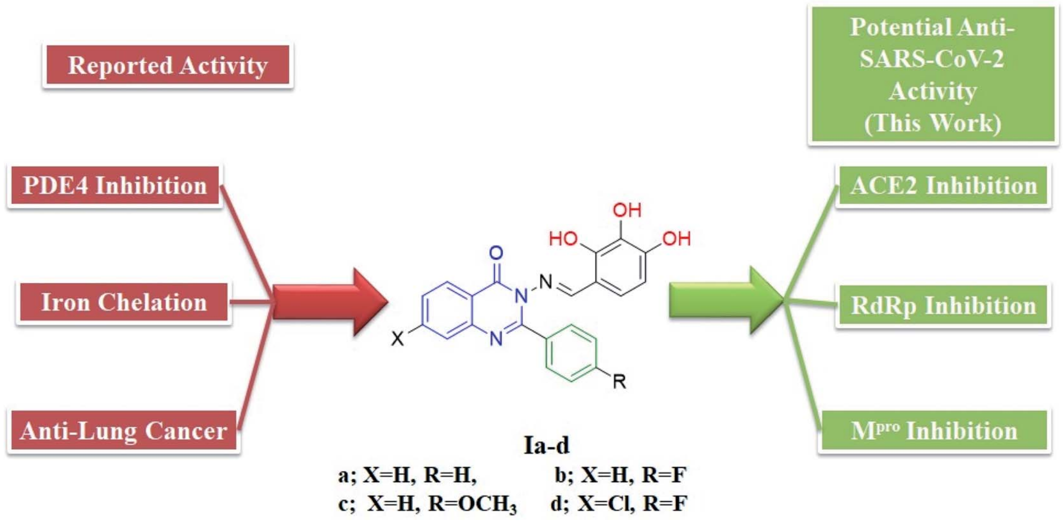

Fig. 4 Structures and rationale for the design of 2-phenylquinazolin-4(3*H*)one-trihydroxyphenyl Schiff base conjugates for COVID-19 therapy.

characterization of all compounds have been reported.[35–37] Briefly, the general methods for the synthesis of compounds **Ia–d** are discussed below. Previous reports suggested the *E* configuration of compounds **Ia–d**.[26] Furthermore, both *Z* and *E* conformers energies were minimized and the calculated total energy of compound **Ic** was 117.266 kcal mol^{-1}, which is lower if it is in *E* configuration (Table 1).

2.1.1. General method for the synthesis of compounds Ia–d.[35–37] Un/substituted benzoyl chloride (0.1 mol) was added portion-wise to an un/substituted anthranilic acid (0.05 mol) dissolved in pyridine in an ice bath (0–5 °C) with stirring until a solid mass formed. The reaction mixture was stirred at room temperature for 30 minutes, and then neutralized with a 20% sodium bicarbonate solution to pH = 7–8. The solid mass was filtered, washed three times with a 20% sodium bicarbonate solution and then distilled water until there was no odor of pyridine, then dried in an oven (70–80 °C), and recrystallized from ethanol (96%) to offer the (un)substituted 2-phenyl-4*H*-benzo[*d*][1,3]oxazin-4-one intermediates.

Then, a mixture of the (un)substituted 2-phenyl-4*H*-benzo[*d*][1,3]oxazin-4-one intermediates (0.1 mol) and hydrazine hydrate 40% (0.1 mol) was refluxed in ethyl alcohol for 4 h. The reaction was monitored with thin layer chromatography (TLC), then poured on crushed ice, filtered, and washed many times with distilled water, dried in an oven (70–80 °C), and then recrystallized from ethanol (96%) to give a fragile solid mass of 3-amino-2-(un)substituted phenylquinazolin-4(3*H*)-one.

Finally, a mixture of the 3-amino-2-(un)substituted phenylquinazolin-4(3*H*)-one intermediates (0.001 mol) and 2,3,4-trihydroxybenzaldehyde (0.001 mol) was refluxed in absolute ethanol with a few drops of glacial acetic acid for 5 h. The reaction was monitored with TLC until completion of the reaction was reached. Then, the solution was cooled and the solid was precipitated, filtered off, dried, and recrystallized from ethanol.

2.2. PDE 4 inhibition assay

PDE assay was performed according to the reported method and detailed results were discussed in our previous work.[35,37] HT-29 cells were harvested from 90–95% confluent 10 cm dishes, and diluted in growth media. The appropriate concentrations of cells were prepared to add 1250 cells in a volume of 25 µL per well in tissue culture treated Griener 384-well microplates, and were then incubated overnight at 37 °C. Experimental compounds were previously diluted to a concentration of 50 mM in DMSO. Concentrated dosing solutions of twice the final concentration were prepared by dilution of the DMSO stocks by 1 : 500 in growth media. Two-fold serial dilutions were then prepared using a medium containing 0.2% DMSO to maintain a constant concentration of the vehicle throughout the concentration range of the compound. Each of these was

Table 1 The values of the total energies of *E* and *Z* isomers of compound **Ic**[a]

Isomer	*E* isomer	*Z* isomer
2D	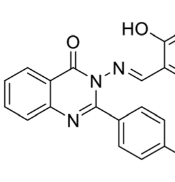 (*E*)-2-(4-methoxyphenyl)-3-(2,3,4-trihydroxybenzylideneamino)quinazolin-4(3*H*)-one	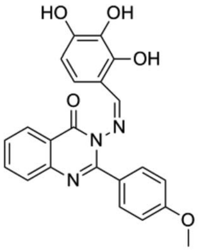 (*Z*)-2-(4-methoxyphenyl)-3-((2,3,4-trihydroxybenzylidene)amino)quinazolin-4(3*H*)-one
3D minimized	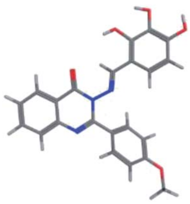	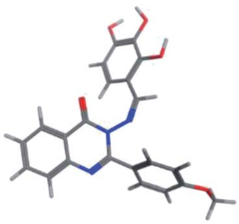
Total energy	117.266	149.139
E_{Str} (bond stretch energy)	8.122	7.595
E_{Ang} (bond angle bend energy)	21.979	42.065
E_{Stb} (stretch-bend energy)	1.966	2.621
E_{Oop} (out-of-plane energy)	0.295	0.417
E_{Tor} (torsion energy)	11.316	15.691
E_{Vdw} (van der Waals energy)	71.813	68.254
E_{Ele} (electrostatics energy)	1.774	12.497

[a] Total energy = $E_{Str} + E_{Ang} + E_{Stb} + E_{Oop} + E_{Tor} + E_{Vdw} + E_{Ele}$.

added in equal volume (25 μL), to four wells on the cell assay plate, along with the vehicle control. Cells were incubated with the compounds for a further 72 h.

At the end of the treatment period, assay plates were allowed to cool to room temperature for 10 min prior to the addition of 25 μL per well of Promega CellTiterGlo reagent, followed by an additional 10 min of incubation at room temperature. The resulting luminescence was quantitated using Molecular Devices Spectramax Paradigm apparatus. The percentage growth inhibition was calculated as follows, where 100% represents the viability of the vehicle treated control samples:

$$100 - \left(100 \times \frac{\text{sample}}{\text{vehicle control}}\right)$$

Thus, on average, the growth inhibition of the vehicle control samples equals zero.

The potency of compounds was determined using a non-linear dose response algorithm (4-parameter logistic fit) with the GraphPad Prism 5 software.

2.3. Docking study

To study the protein–ligand interactions, compounds were sketched using Marvin sketch powered by Chem-Axon and then transferred to a Molecular Operating Environment (MOE) platform to undergo energy optimization for each compound using the MMFF94x forcefield (with the gradient set to root mean square (RMS) 0.1 kcal mol^{-1}). The crystallographic 3D protein structures of SARS-CoV-2 RdRp in a complex with cofactors (PDB ID: 6M71), the crystal structure of the SARS-CoV-2 spike receptor-binding domain bound to ACE2 (PDB ID: 6M0J) and the crystal structure of the SARS-CoV-2 main protease M$^{\text{pro}}$ in a complex with Z1220452176 (PDB ID: 5R7Z) were obtained from the RSCB protein data bank (http://www.rscb.org). Molecular docking was conducted using the MOE 2020.0101 package. Visualization and generation of the 3D figures were performed using PyMOL 2.4 software.

2.4. Molecular dynamics simulations

The conformational stability of the protein–ligand interactions was evaluated using molecular dynamics (MD) simulations analysis performed using MOE software. In this work, the MD of the ligands were studied using Nosé–Poincaré–Andersen (NPA), which is the most precise and the most sensitive. In MD calculations, an AMBER10:EHT force field, sphere shape, water as a solvent, six margins and the deletion of solvent molecules at a distance of greater than 4 Å were selected to optimize the system.

2.5. Prediction of the pharmacokinetic properties and toxicological properties using ADMET

For the calculation of the pharmacokinetic properties of the compounds under study, online pkCSM pharmacokinetics prediction properties were used.[38] The following properties, (i) absorption, Lipinski's rule of five, water solubility, Caco-2 permeability, intestinal absorption (human), skin permeability and P-glycoprotein interactions, (ii) distribution: VDss, Fu, Log BB and CNS permeability, (iii) metabolism and (iv) excretion were selected.

Also, online pkCSM pharmacokinetics were used to predict the toxicity of the molecules, including skin sensitization, hepatotoxicity, *etc.* The results obtained were analyzed and compared with the reference values of the pkCSM pharmacokinetics prediction properties.[39]

3. Results and discussion

3.1. PDE 4 inhibition assay

Compounds **Ia–d** were screened *in vitro* for their inhibition of PDE 4B in our previous study using rolipram, a positive reference drug,[37] and also, the mentioned compounds were evaluated for their anticancer activity.[40] The screening was performed at 10 μM in triplicate and the results revealed that all compounds have significant inhibitory activity (% inhibition = 56, 85, and 89, respectively). Structure activity correlation showed that 2,3,4-trihydroxy moiety that served as a hydrogen bond donor may be responsible for the PDE 4B inhibitory activity of the compounds. Additionally, the presence of a 7-Cl at the quinazolinone ring in compound **Id** further improved the inhibitory effect (% inhibition = 89). These results may suggest the possibility of repurposing these synthesized quinazolinone derivatives as multi-target inhibitors against coronavirus.

3.2. Docking results

3.2.1. Docking of target compounds against SARS-CoV-2 spike receptor-binding domain bound with ACE2. ACE2 plays vital roles ranging from catalytic activities with various substrates as a functional receptor for COVID-19 disease and as an amino acid transporter.[41–44] The difference between SARS-CoV-2 and the original SARS-CoV is 380 amino acid substitutions. These amino acid substitutions translate to differences in five of the six vital amino acids in the receptor-binding domain between the viral spike (S) protein and surface expressed human ACE2.[45] Thus, viral spike glycoproteins are well represented as a significant determinant of host tropism and are a key target for therapeutic development.

The crystal structure of the SARS-CoV-2 spike receptor-binding domain bound with ACE2 (PDB ID: 6M0J) contains two chains, where chain A represents the angiotensin-converting enzyme 2 structure of homo sapiens and chain E is the spike receptor binding domain.[46]

Recently, a library of ligands comprising 30 phytochemicals from medicinal plants was prepared for docking. The best compound, silybin (flavonolignan), scored −10.572 kcal mol^{-1} with a Silybin-S spike glycoprotein complex forming hydrogen bonds with residues His34, Arg403, Tyr453, Ser494 and Lys353 present in this pocket.[47]

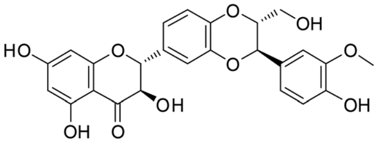

Silybin (flavonolignan)

Table 2 Binding energy score of the target compounds with SARS-CoV-2 spike receptor-binding domain bound ACE2 (PDB ID: 6M0J)

	Crystal structure of SARS-CoV-2 spike receptor-binding domain bound with ACE2 (PDB ID: 6M0J)				
Compound	Affinity, kcal mol^{-1}	Distance (in Å) from main residue		Functional group	Interaction
Ia	−15.8821	2.54	His34	Phenyl ring	Pi–cation
		2.14	Arg403	*N* of Schiff base	H-acceptor
		3.07	Ala387	Phenolic OH	H-donor
Ib	−16.3852	2.82	His34	Phenolic OH	H-donor
		2.93	Arg403	Quinazoline ring	Pi–cation
Ic	−16.8866	2.19	His34	Cyclic C=O	H-acceptor
		2.21	His34	*N* of Schiff base	H-acceptor
		3.86	His34	Phenyl ring	Pi–pi
		3.03	Ser494	Quinazoline ring	Pi–H
Id	−16.3282	2.91	His34	Phenolic OH	H-donor
		2.71	Arg403	*N* of Schiff base	H-acceptor
Ic metabolite	−12.1711	2.35	His34	Quinazoline ring	Pi–H
		2.24	His34	Quinazoline ring	Pi–cation
		3.02	Ala387	Phenolic OH	H-donor

Compound **Ic** exhibits a minimum binding energy −16.8866 kcal mol^{-1} by targeting His34 and Ser49 *via* hydrogen bonding, π–π and π–H interactions (Table 2). Furthermore, compound **Ia** shows significant binding interactions to SGp chain E; a spike glycoprotein that plays a vital role in attaching the virus to the human receptor ACE2 cell membrane. Thus, blockage of SGp reduces the binding of the virus to the host. Also, compound **Ib** exhibits hydrogen bonding and hydrophobic interactions with His34 and Arg403 amino acid residues in the same binding site as the ligand (Fig. 5). These interactions seem to inhibit the functions of SGp, thus achieving blockage of the SGp functional protein suppresses the activity of binding to the host. It is worth mentioning that ACE2 is responsible for altering the sensitivity of both the substrate and the inhibitor by binding to the cavity of chain B. Additionally, both π–alkyl and van der Waals interactions can reduce the binding capabilities of the virus, which enables target compounds with antioxidant activity and thus more inhibitory action. Compound **Ic** has a methoxy group that can be hydrolyzed inside the body, therefore its metabolite was redocked to predict its inhibitory activity. The results revealed that the metabolite reserve the initial π–π interactions with the His34 amino acid residue. Moreover, it binds *via* a hydrogen bond donor with Ala387, with a binding energy of −12.1711 kcal mol^{-1}.

Interestingly, the Schiff moiety formed interactions with His34 or Arg403 residues as a hydrogen bond acceptor and this may serve as a useful pharmacophoric feature for designing more active agents.

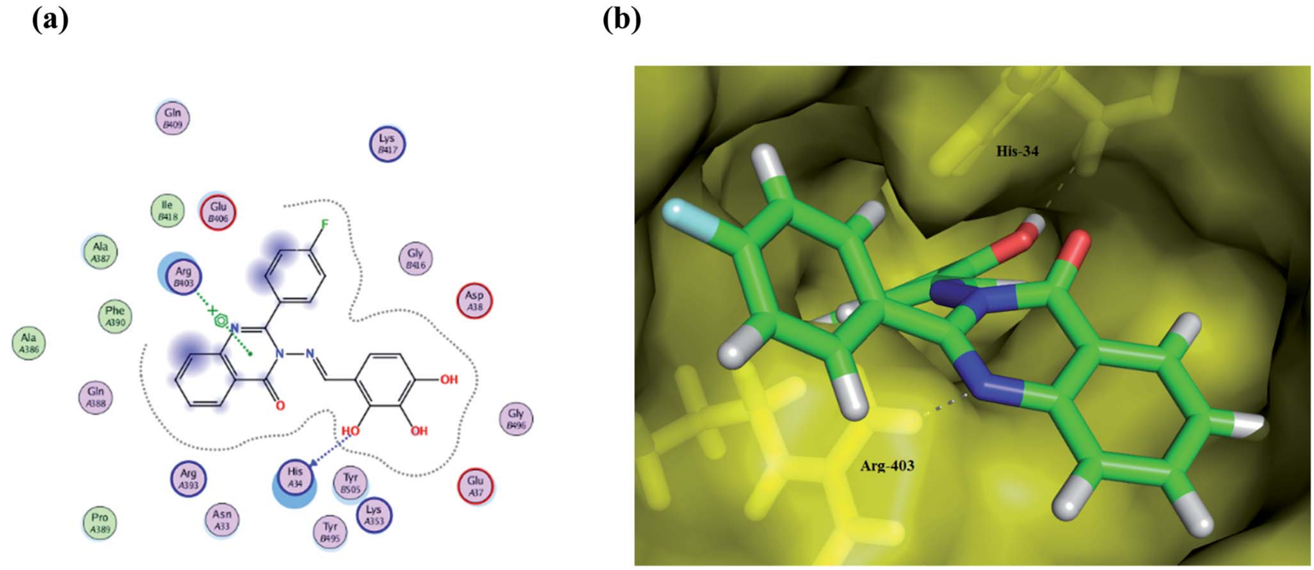

Fig. 5 (a) A 2D animated structure showing the binding interactions between compound **Ib** and SGp and (b) a 3D representation showing the position of compound **Ib** within the cavity of SGp.

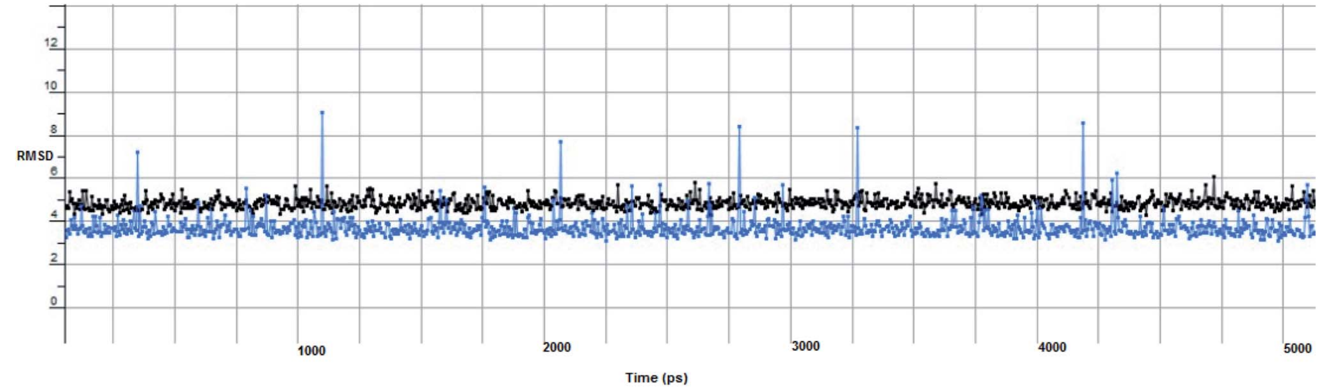

Fig. 6 The RMSD curve from the molecular dynamics simulation of compound **Ic**. The *x*-axis represents the simulation time (in ps), while the *y*-axis represents the RMSD value (in nm).

In computational drug discovery, MD is a technique that sheds light on the allosteric binding site of the protein, and conformation of the ligand–protein complex. Also, it can simulate the conditions that are hard to perform under in wet experiments. Herein, compound **Ic** was subjected to MD simulations bound to the SARS-CoV-2 spike receptor-binding domain bound with ACE2. It can be seen from Fig. 6 that compound **Ic** retained its binding affinity and firmly bound to its respective binding site. The root mean square deviation (RMSD) value produced in the compound **Ic** complex was stable at 0.6 nm.

3.2.2. Docking of target compounds against SARS-CoV-2 main protease. The main protease of coronaviruses is an enzyme that participates in the viral replication, cleaving the polyprotein. M^{pro} is a cysteine protease that consists mainly of three domains and is active in a homodimer form.[48] The catalytic dyad of Cys145 and His41 present in the cleft between domains I and II in addition to Glu166 residue are involved in protein dimerization. Also, this catalytic dyad of Cys145 and His41 respectively formed π–alkyl and π–π T-shaped interactions.[33] The crystal structure of the SARS-CoV-2 main protease in complex with Z1220452176 (PDB ID: 5R7Z) contains chain A, representing 3C-like proteinase co-crystallized with HWH. To ensure the validity of the docking protocol, re-docking of the co-crystallized native ligand into the active site was performed. The coordinates of the best scoring docking pose of the native ligand were compared with its coordinates in the co-crystallized PDB file based on the binding mode and RMSD. The re-docked ligand showed an RMSD of 0.7021 Å between the docked pose and the co-crystallized ligand (energy score (S) = -9.230 kcal mol^{-1}). In line with the examination of the active site, recent studies have mentioned that the active site of this protein contains Glu166 as the most repeated and important residue, alongside Gln189, His41 and Thr190.[34] The results of docking procedures represented in Table 3 reveal that all of the compounds showed remarkable affinity to the selected pocket according to their affinity in kcal mol^{-1}. It is important to mention that for M^{pro} simulation, the fluctuation impact at the chain A residues (5–16, 46–56, 136–151, 165–178, 181–196, 241–260, 271–286), indicates the ligand interactions at these

Table 3 Binding energy score of the target compounds with SARS-CoV-2 main protease in complex with Z1220452176 (PDB ID: 5R7Z)

	Crystal structure of SARS-CoV-2 main protease in complex with Z1220452176 (PDB ID: 5R7Z)				
Compound	Affinity, kcal mol^{-1}	Distance (in Å) from main residue		Functional group	Interaction
Ia	−13.3909	2.42	Glu166	Phenolic OH	H–donor
		2.66	His41	Phenyl ring	H–pi
Ib	−12.7504	3.25	Glu166	Quinazoline ring	H–donor
		2.12	Thr190	Phenolic OH	Pi–H
Ic	−13.5962	2.44	Glu166	Phenolic OH	H–donor
		2.89	Glu166	Phenolic OH	H–donor
		3.17	Gln189	Quinazoline ring	Pi–H
		3.04	Gln189	Quinazoline ring	Pi–H
Id	−13.0212	2.83	Glu166	Phenolic OH	H–donor
		2.89	Glu166	Phenolic OH	H–donor
		2.99	Gln189	Phenyl ring	Pi–H
Ic metabolite	−10.3634	2.21	Glu166	Phenolic OH	H–donor
		3.12	Gln189	Phenyl ring	Pi–H

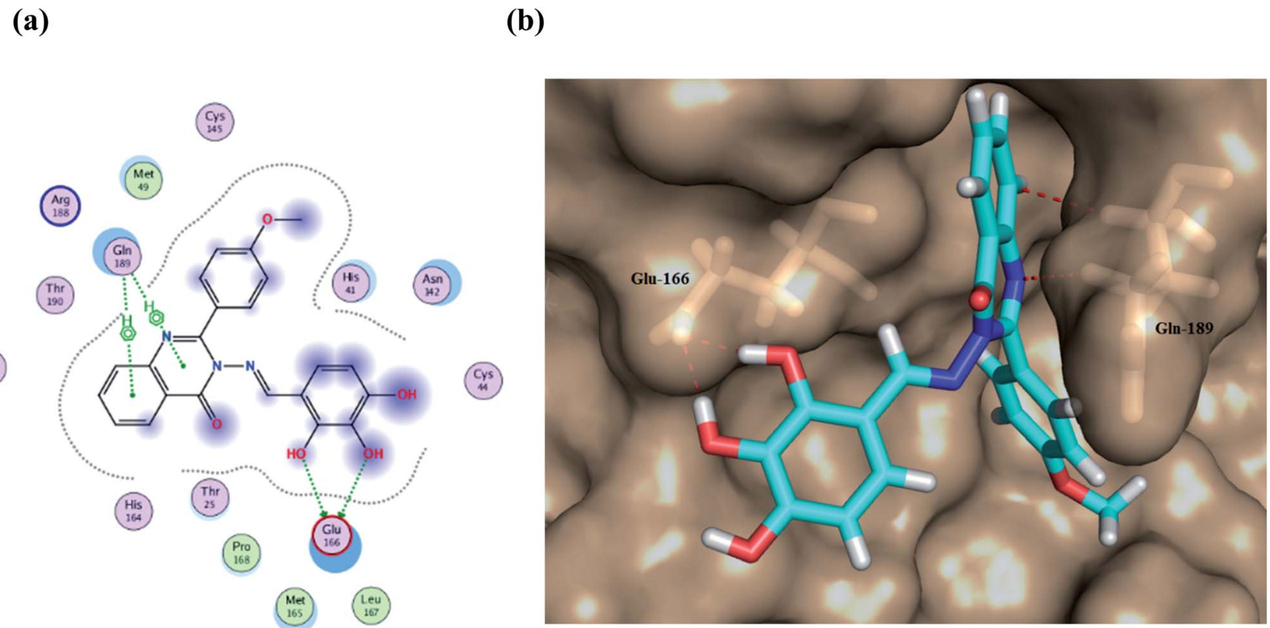

Fig. 7 (a) A 2D animated structure showing the binding interactions between compound **Ic** and M^{pro} and (b) a 3D representation showing the position of compound **Ic** within the cavity of M^{pro}.

residues. Thus, compound **Ic** seemed to bind firmly at the active site of the M^{pro} long loop region of domain II with the quinazoline ring deeply embedded in the S1 pocket. Our *in silico* docking study shows that the screened compounds interact with Glu 166 (also forming strong hydrogen bonding), Gln 189, His 41, and Thr 190 and share the same binding pocket similar to the ligand, which reveals the potent inhibition of the virus protease.

Furthermore, two hydrogen bond donations to the main chain of Glu166 and π–H interactions to the Gln 189 amino acid, with a binding energy of -13.5962 kcal mol^{-1} (Fig. 7), were calculated. Also, the other tested compounds showed comparable binding interactions to main amino acids; Glu 166, Gln 189, His 41 and Thr 190; which seemed to be useful in the inhibition of the enzyme. So, a tri-hydroxy moiety alongside a quinazoline scaffold may serve as excellent binding features to inhibit this enzyme. Regarding the metabolite analogue of derivative **Ic**, it reserves the same hydrophobic and hydrogen bonding interaction with the Glu166 and Gln 189 amino acid residues, respectively. In the MD simulation, compound **Ic** retained its binding affinity and still firmly bound to the respective binding site. The average RMSD value of the ligand relative to the initial structure was around 0.7 Å and increased up to 3.9 Å without losing the key interactions and staying stable for the rest of the MD simulations (Fig. 8).

3.2.3. Docking of target compounds against SARS-CoV-2 RNA-dependent RNA polymerase (RdRp). SARS-Cov-2 RNA-dependent RNA polymerase in a complex with cofactors (PDB ID: 6M71) is a catalytic RNA that contains four chains, in which chain A represents the SARS-Cov-2 structure of nonstructural protein 12 known as NSP12, chain C can be attributed to NSP8 and chains B and D both represent NSP7.[49] The NTP entry channel is formed by a set of hydrophilic residues, Lys545, Arg553, and Arg555. The RdRp active site is located in a tunnel

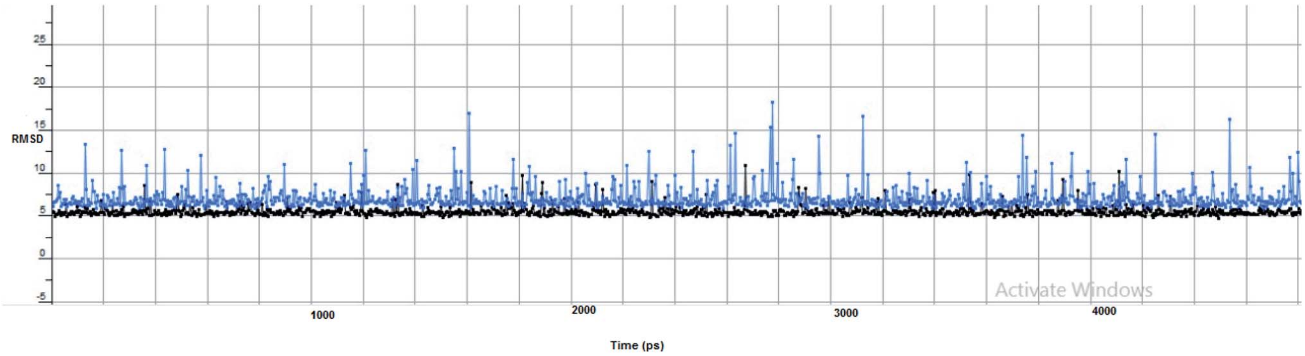

Fig. 8 The RMSD curve from the molecular dynamics simulation of compound **Ic**. The *x*-axis represents the simulation time (in ps), while the *y*-axis represents the RMSD value (in nm).

Table 4 Binding energy score of the target compounds with SARS-CoV-2 RNA-dependent RNA polymerase (PDB ID: 6M71)

	SARS-Cov-2 RNA-dependent RNA polymerase (PDB ID: 6M71)				
Compound	Affinity, kcal mol^{-1}	Distance (in Å) from main residue		Functional group	Interaction
Penciclovir	−14.5929	2.63	Thr556	–NH_2	H–donor
		2.71	Thr556	*N* of diazine	H–acceptor
		2.89	Arg553	Cyclic C═O	H–acceptor
		2.14	Arg 555	Cyclic C═O	H–acceptor
			Arg555	*N* of Diazole	H–acceptor
Ia	−14.0245	3.02	Thr556	Phenolic OH	H–donor
		2.99	Thr556	Phenolic OH	H–acceptor
		3.19	Cys622	Quinazoline ring	Pi–H
Ib	−13.8649	2.96	Thr556	Phenolic OH	H–donor
		2.70	Thr556	Phenolic OH	H–donor
		2.98	Arg553	Cyclic C═O	H–acceptor
		2.98	Arg555	Cyclic C═O	H–acceptor
Ic	−14.6145	2.93	Cys622	Cyclic C═O	H–acceptor
		2.94	Asp452	phenolic OH	H–donor
		3.09	Lys621	Quinazoline ring	Pi–H
		3.17	Tyr619	Quinazoline ring	Pi–H
Id	−12.9652	2.81	Thr556	Phenolic OH	H–donor
		2.73	Lys621	Quinazoline ring	H–donor
		3.18	Asp618	–Cl	Halogen bond
Ic metabolite	−14.5929	3.71	Arg553	–Phenyl ring	Pi–cation
		3.61	Arg555	–Phenyl ring	Pi–cation

shape, where the protein complex with strong electrostatic surfaces contains divalent cationic residues 611–626, especially residue Asp618. Some catalytic residues are also located between residues 753–769. The amino acid sequence of the non-structural proteins (NSP12) of SARS-CoV-2 shows that RdRp domain contains three sub-domains and seven motifs (A–G), with no co-crystallized ligand.[50] Docking of the tested synthesized compounds with the NSP12 structure that dominates the RNA-dependent RNA polymerase activity of SARS-CoV-2 can be attributed as one of the significant therapeutic targets for coronaviruses. Thus, the chains containing NSP7 and NSP8 residues were removed from the PDB file.[51] Among the 43 approved drugs docked into NSP12 SARS-Cov-2 by generating the lowest energetic pose of the ligand and protein, Penciclovir,

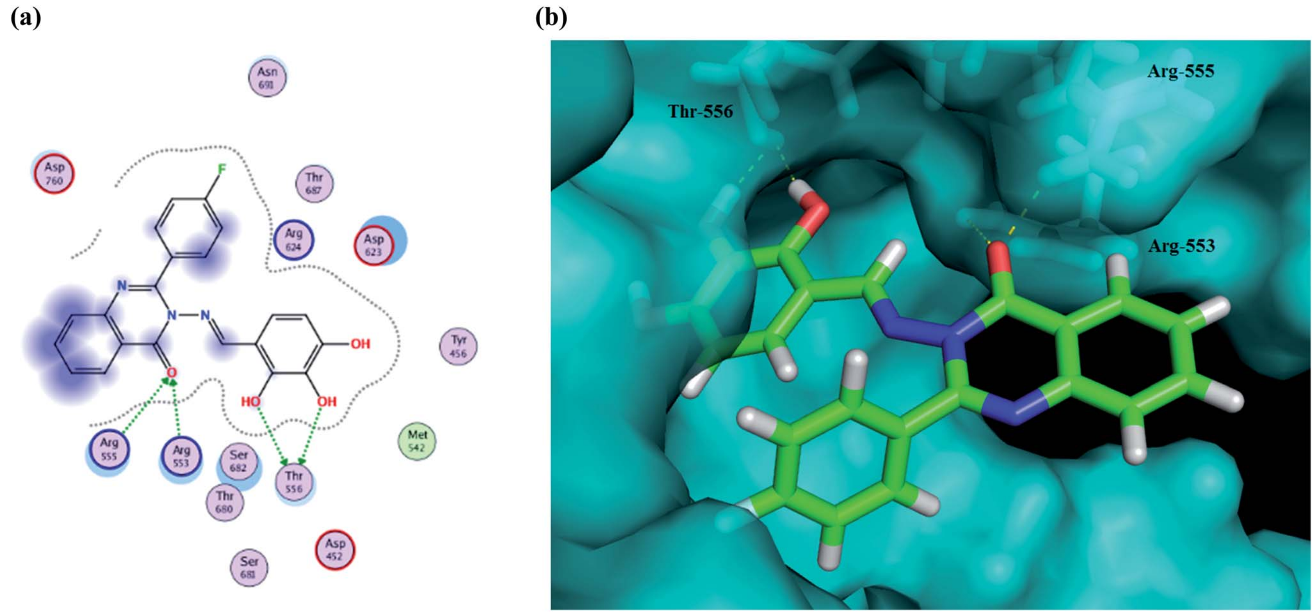

Fig. 9 (a) 2D animated structure showing the binding interactions between compound **Ib** and RdRp and (b) a 3D representation showing the position of compound **Ib** within the cavity of RdRp.

which is structurally closer to the synthesized quinazolinone derivatives, showed a significant docking score of −14.59 kcal mol^{-1}. Penciclovir binds to motifs A and F and forms interactions with theThr556, Arg553 and Arg555 residues.[50] Also, in a recent study, Ahmad *et al.* reported that Arg553, Pro620, and Asp618 may be involved in binding interactions in the inhibition of RdRp.[52]

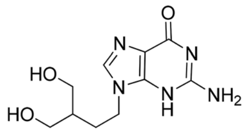

Penciclovir

The active site containing these amino acids was chosen using the site finder properties of MOE 2020.0101. All the target compounds bind at the RdRp functional sites, with a high docking score and the interaction details and the binding energy of the four quinazoline derivatives **Ia–d** at the active site of RdRp are summarized in Table 4.

The results show that all of the compounds have excellent affinity to the selected pocket, according to the affinity in kcal mol^{-1}. The synthesized derivative **Ib** is encapsulated in the receptor cavity with a binding energy score of −13.8649 kcal mol^{-1}. The binding site is located between the NiRAN domain and β-hairpin structure that polymerizes the 3′ end,[49] and therefore it may interfere with the polymerizing activity. The mentioned derivative binds firmly to amino acids residues Thr556, Arg553, Arg555 (Fig. 9). Also, compound **Id** forms a non-covalent interaction with the divalent cationic residue of Asp618. The potent synthesized derivative was docked at the active site between the NSP12-NSP7 residues forms conventional hydrogen bonds to Asp452, and van der Waals interactions with residues Tyr619 and Lys621, including π–alkyl/π–πcontacts with residue Cys622 located in the RdRp tunnel structure. Notably, that tri-hydroxy moiety plays a significant role in these interactions as it forms hydrogen bond interactions with the Thr556 and Asp452 amino acid residues. All these interactions between the trihydroxy moiety and RdRp may serve as a crucial pharmacophore for further development of more potent target derivatives. Moreover, the interactions of the **Ic** metabolite analogue were examined and it was shown that it forms π–cation interactions with Arg 553 and Arg 555. The distances and energy bindings are presented in Table 4.

The proposed inhibitor **Ic** for SARS-CoV-2 identified as a result of molecular docking against RdRp was further investigated to determine its binding mode stability at the active site through MD simulations studies. The preliminary analysis performed on MD trajectory files was RMSD. The RMSD analysis was performed on the backbone atoms of the proteins (both in complex and free state) and average RMSD values obtained for ligand bound proteins (*i.e.* the inhibitor protein complex) were ∼0.8 Å, establishing their overall stability over the explored timescale, as shown in Fig. 10.

3.3. Predication of the pharmacokinetic properties and toxicological properties *via* ADMET

In this study, the pharmacokinetic predictions of the quinazolinone Schiff base conjugates (**Ia–d**) were estimated. The results revealed that all the investigated molecules show significant values for oral absorption. Compound **Ic** shows the highest water solubility value among the other analogues. All of the evaluated compounds are predicted to have high cellular permeability, especially for intestinal cells (91.62–99.16%) (Table 5). Generally, it is known that an orally available molecule that satisfies both Lipinski's and Veber's rules has a balance between lipophilicity and hydrophilicity. As shown from Table 6, compounds **Ia–d** follow both Lipinski's and Veber's rules and thus qualify as possible drug-like molecules. Furthermore, the observed lipophilicities correlate negatively with the water solubility potentials of the target compound but have an association with the Caco2 permeability. This corresponds to the reported observation that there was no correlation between the lipophilicity and drug permeability measured using the human colon adenocarcinoma (Caco-2) cell line assay reported previously.[53] Prediction of the distribution properties showed that compound **Id** shows the highest blood–brain barrier (BBB) permeability and unbound fraction among the

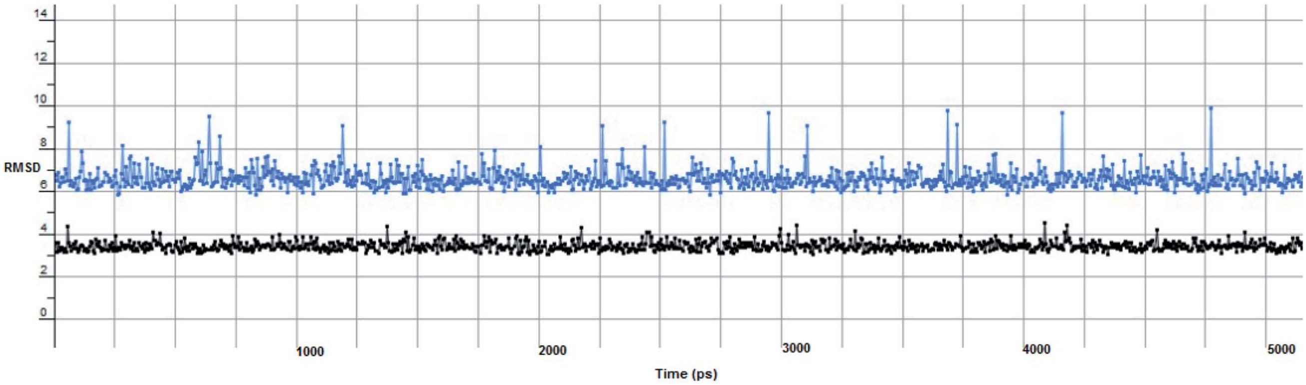

Fig. 10 The RMSD curve from the molecular dynamics simulation of compound Ic. The *x*-axis represents the simulation time (in ps), while the *y*-axis represents the RMSD value (in nm).

Table 5 ADMET properties of the target synthesized compounds

Property		Compound **Ia**	Compound **Ib**	Compound **Ic**	Compound **Id**
Absorption	Water solubility (log mol L^{-1})	−3.602	−3.515	−3.955	−3.603
	Caco2 permeability (log Papp in 10^{-6} cm s^{-1})	0.024	0.091	0.064	0.014
	Intestinal absorption (%)	91.625	97.956	94.345	99.161
	Skin permeability (log K_p)	−2.735	−2.735	−2.735	−2.735
	P-Glycoprotein substrate	Yes	Yes	Yes	Yes
	P-Glycoprotein I	Yes	Yes	Yes	Yes
	P-Glycoprotein II	Yes	Yes	Yes	Yes
Distribution	VDss (log L kg^{-1})	−1.021	−0.92	−1.179	−0.831
	Fraction unbound (Fu)	0.087	0.137	0	0.14
	BBB permeability (log BB)	−1.1	−1.327	−1.41	−1.5
	CNS permeability (log PS)	−2.339	−3.14	−3.371	−3.068
Metabolism	CYP2D6 substrate	No	No	No	No
	CYP3A4 substrate	Yes	Yes	Yes	Yes
	CYP1A2 inhibitor	Yes	Yes	Yes	Yes
	CYP2C19 inhibitor	Yes	Yes	Yes	Yes
	CYP2C9 inhibitor	Yes	Yes	Yes	Yes
	CYP2D6 inhibitor	Yes	Yes	No	Yes
	CYP3A4 inhibitor	No	No	Yes	Yes
Excretion	Total clearance (log ml mim^{-1} kg^{-1})	0.385	0.239	0.325	−0.1
	Renal OCT2 substrate	No	No	No	No
Toxicity	AMES toxicity	Yes	Yes	No	No
	Max. tolerated dose (log mg kg^{-1} day^{-1})	0.44	0.492	0.343	0.495
	hERG I inhibitor	No	No	No	No
	hERG II inhibitor	Yes	Yes	Yes	Yes
	Oral rat acute toxicity (LD_{50}) (mol kg^{-1})	2.627	2.513	2.706	2.533
	Oral rat chronic toxicity (LOAEL) (mol kg^{-1} bw day^{-1})	3.527	2.595	3.504	2.541
	Hepatotoxicity	Yes	Yes	Yes	Yes
	Skin sensitisation	No	No	No	No
	T. pyriformis toxicity (log μg L^{-1})	0.287	0.286	0.286	0.286
	Minnow toxicity (log mM)	0.155	0.002	−0.98	−0.515

other analogues (Table 5). The quinazoline derivatives were predicted to be substrates of P-glycoprotein, which is a member of the ATP-binding cassette transporter found primarily in epithelial cells. Thus, this can be explained by the ability of these compounds to modulate the physiological functions of P-glycoprotein in limiting the active uptake and distribution of these compounds. All of the synthesized compounds showed relatively high activity as they inhibit CYP2C19, CYP2C9, CYP2D6, and CYP3A4. This can be positively correlated to the lipophilicity of the compounds to metabolism related toxicity. These results show that these compounds could be involved in drug–drug interactions, and could initiate oxidative stress. It was observed that there were no remarkable difference in the parameters related to metabolism and excretion among the four analogues, except for the unsubstituted **Ia** and methoxy **Ic** derivatives, which showed a higher total clearance relative to the others. In conclusion, in this study, pkCSM software was used to predict the toxicological properties of the target compounds. Furthermore, this software has a system that performs predictions on the type of toxicity that a compound presents, such as mutagenicity, hepatotoxicity, cardiotoxicity, and skin sensitization. Herein, the bacterial mutagenic potential of the quinazoline derivatives through Ames toxicity testing showed that two analogues, namely **Ic** and **Id**, could be

Table 6 Lipinski's and Veber's for the synthesized target compounds

Property	Compound **Ia**	Compound **Ib**	Compound **Ic**	Compound **Id**
log *P*	3.06	3.20	3.07	3.85
Molecular weight	373.37	391.36	403.39	425.80
NORTB	3	3	4	3
H-bond acceptors	7	7	8	7
H-bond donor	3	3	3	3
No. of Lipinski's rule violations	0	0	0	0
TPSA	158.65	162.82	170.13	173.120

considered as non-mutagenic agents. Yet, the toxicities of all of the compounds in *T. pyriformis* are high. Also, the investigated compounds were predicted for one of the important parameters regarding toxicity, which is cardiotoxicity, in the form of human ether-a-go-go-related gene I (hERG I), which was found to be at an acceptable level.

4. Conclusions

Designing effective small-molecule therapeutics promises to be the fastest therapeutic way to stem the tide of the COVID-19 pandemic. Therefore, a series of previously synthesized quinazoline Schiff base conjugates designed as PDE 4B inhibitors was *in silico* examined for possible ability to stop SARS-CoV-2 viral infection *via* several mechanisms. Docking studies results revealed that the Schiff moiety may inhibit the spike glycoprotein, while the tri-hydroxy group alongside a quinazoline ring may serve as a good scaffold to inhibit both M^{pro} and RdRp enzymes. Compound **Ib** was found to fit the substrate binding site and presents strong interactions with the mentioned targets. The binding stability of compound **1c** inside the pocket of the mentioned proteins with time was further validated through molecular dynamic simulations involving root mean square deviation. Furthermore, ADMET properties were calculated and showed satisfactory pharmacokinetic and toxicological properties. Therefore, combining the docking results, ADMET predictions and the biological activity of the studied quinazoline conjugates as PDE 4B inhibitors, we suggest that these compounds can be further studied as suitable therapeutic treatments for COVID-19.

Conflicts of interest

No potential conflicts of interest are reported by the authors.

Acknowledgements

The authors thank Nahda University in Beni Suef (NUB) for supporting this work.

References

1 S. Jiang, Z. Shi, Y. Shu, J. Song, G. F. Gao, W. Tan and D. Guo, *Lancet*, 2020, **395**, 949.

2 V. M. Corman, D. Muth, D. Niemeyer and C. Drosten, *Adv. Virus Res.*, 2018, **100**, 163.

3 T. P. Velavan and C. G. Meyer, *Trop. Med. Int. Health*, 2020, **25**, 278.

4 P. Liu, W. Chen and J. P. Chen, *Viruses*, 2019, **11**, 979.

5 M. Hagar, H. A. Ahmed, G. Aljohani and O. A. Alhaddad, *Int. J. Mol. Sci.*, 2020, **21**, 3922.

6 D. Gentile, V. Patamia, A. Scala, M. T. Sciortino, A. Piperno and A. Rescifina, *Mar. Drugs*, 2020, **18**, 225.

7 O. O. Olubiyi, M. Olagunju, M. Keutmann, J. Loschwitz and B. Strodel, *Molecules*, 2020, **25**, 3193.

8 S. T. Ngo, N. Q. A. Pham, L. T. Le, D.-H. Pham and V. V. Vu, *J. Chem. Inf. Model.*, 2020, DOI: 10.1021/acs.jcim.0c00491.

9 L. Zhang, D. Lin, X. Sun, U. Curth, C. Drosten, L. Sauerhering, S. Becker, K. Rox and R. Hilgenfeld, *Science*, 2020, **368**, 409.

10 W. R. Ferraz, R. A. Gomes, A. L. S Novaes and G. H. G. Trossini, *Future Med. Chem.*, 2020, DOI: 10.4155/fmc-2020-0165.

11 M. S. Yu, J. Lee, J. M. Lee, Y. Kim, Y. W. Chin, J. G. Jee and Y. J. Jeong, *Bioorg. Med. Chem. Lett.*, 2012, **22**, 4049.

12 Y. Kumar, H. Singh and C. N. Patel, *J. Infect. Public Health*, 2020, DOI: 10.1016/j.jiph.2020.06.016.

13 S. Shahinshavali, K. A. Hossain, A. V. D. N. Kumar, A. G. Reddy, D. Kolli, A. Nakhi, M. V. B. Rao and M. Pal, *Tetrahedron Lett.*, 2020, 152336.

14 R. Alexpandi, J. F. De Mesquita, S. K. Pandian and A. V. Ravi, *Front. Microbiol.*, 2020, **11**, 1796.

15 A. K. Ghosh, M. Brindisi, D. Shahabi, M. E. Chapman and A. D. Mesecar, *ChemMedChem*, 2020, **15**, 907.

16 M. Dalamaga, I. Karampela and C. S. Mantzoros, *Metabolism*, 2020, **109**, 154282.

17 Z. Varga, A. J. Flammer and P. Steiger, *Lancet*, 2020, **395**, 1417.

18 J. Luan, Y. Lu, X. Jin and L. Zhang, *Biochem. Biophys. Res. Commun.*, 2020, **526**, 165.

19 M. Gheblawi, K. Wang, A. Viveiros, Q. Nguyen, J. C. Zhong, A. J. Turner, M. K. Raizada, M. B. Grant and G. Y. Oudit, *Circ. Res.*, 2020, **126**, 1457.

20 T. Hirschhorn and B. R. Stockwell, *Free Radic. Biol. Med.*, 2019, **133**, 130.

21 W. Liu, S. Zhang, S. Nekhai and S. Liu, *Curr. Clin. Microbiol. Rep.*, 2020, **7**, 13.

22 D. TangI, P. ComishID and R. Kang, *PLoS Pathog.*, 2020, **16**, 1008536.

23 D. C. Hall and H.-F. Ji, *Trav. Med. Infect. Dis.*, 2020, **35**, 101646.

24 R. T. Eastman, J. S. Roth, K. R. Brimacombe, A. Simeonov, M. Shen, S. Patnaik and M. D. Hall, *ACS Cent. Sci.*, 2020, **6**, 672.

25 A. Cavezzi, E. Troiani and S. Corrao, *Clin. Pract.*, 2020, **10**, 1271.

26 J. E. Phillips, *Front. Pharmacol.*, 2020, **11**, 259.

27 H. Li, J. Zuo and W. Tang, *Front. Pharmacol.*, 2018, **9**, 1048.

28 A. Kodimuthali, S. S. L. Jabaris and M. Pal, *J. Med. Chem.*, 2008, **51**, 5471.

29 R. Sunke, R. Bankala, B. Thirupataiah, E. V. V. Shivaji Ramarao, J. S. Kumar, H. M. Doss, R. Medishetti, P. Kulkarni, R. K. Kapavarapu, M. Rasool, J. Mudgal, J. E. Mathew, G. G. Shenoy, K. V. L. Parsa and M. Pal, *Eur. J. Med. Chem.*, 2019, **174**, 198–215.

30 M. Dalamaga, I. Karampela and C. S. Mantzoros, *Metabolism*, 2020, **109**, 154282.

31 S. Jo, H. Kim, S. Kim, D. H. Shin and M. S. Kim, *Chem. Biol. Drug Des.*, 2019, **94**, 2023.

32 S. Jo, S. Kim, D. H. Shin and M. S. Kim, *J. Enzyme Inhib. Med. Chem.*, 2020, **35**, 145.

33 S. Vardhan and S. K. Sahoo, *Comput. Biol. Med.*, 2020, **124**, 103936.

34 A. M. Sayed, A. R. Khattab, A. M. AboulMagd, H. M. Hassan, M. E. Rateb, H. Zaid and U. R. Abdelmohsen, *RSC Adv.*, 2020, **10**, 19790.

35 H. M. Abdel-Rahman, M. Abdel-Aziz, J. C. Canzoneri, B. D. Gary and G. A. Piazza, *Arch. Pharm.*, 2014, **347**, 650.

36 K. S. Kumar, S. Ganguly, R. Veerasamy and E. De Clercq, *Eur. J. Med. Chem.*, 2010, **45**, 5474.

37 M. Mansour, M. T. El-Saadi, N. H. Amin, J. Canzoneri, A. Keeton, G. Piazza and H. M. Abdel-Rahman, *Egypt. J. Chem.*, 2020, DOI: 10.21608/ejchem.2020.28992.2624.

38 Pharmacokinetic properties, http://biosig.unimelb.edu.au/pkcsm/prediction.

39 D. E. Pires, T. L. Blundell and D. B. Ascher, *J. Med. Chem.*, 2015, **58**, 4066.

40 S. F. El-Menshawe, O. M. Sayed, H. A. Abou Taleb, M. A. Saweris, D. M. Zaher and H. A. Omar, *J. Drug Deliv. Sci. Technol.*, 2020, 101569.

41 W. Li, M. J. Moore, N. Vasilieva, J. Sui, S. K. Wong, M. A. Berne, M. Somasundaran, J. L. Sullivan, K. Luzuriaga and T. C. Greenough, *Nature*, 2003, **426**, 450.

42 A. J. Turner, J. A. Hiscox and N. M. Hooper, *Trends Pharmacol. Sci.*, 2004, **25**, 291.

43 N. E. Clarke and A. J. Turner, *Int. J. Hypertens.*, 2012, **2012**, 307315.

44 T. Hashimoto, T. Perlot, A. Rehman, J. Trichereau, H. Ishiguro, M. Paolino, V. Sigl, T. Hanada, R. Hanada and S. Lipinski, *Nature*, 2012, **487**, 477.

45 A. Wu, Y. Peng, B. Huang, X. Ding, X. Wang, P. Niu, J. Meng, Z. Zhu, Z. Zhang and J. Wang, *Cell Host Microbe*, 2020, **27**, 325.

46 J. Lan, J. Ge, J. Yu, S. Shan, H. Zhou, S. Fan and X. Wang, *Nature*, 2020, **581**, 215.

47 A. C. Walls, Y. J. Park, M. A. Tortorici, A. Wall, A. T. McGuire and D. Veesle, *Cell*, 2020, **180**, 281.

48 S. Ekins, M. Mottin, P. R. Ramos, B. K. Sousa, B. J. Neves, D. H. Foil and A. C. Puhl, *Drug Discov. Today*, 2020, **25**, 928.

49 Y. Gao, L. Yan, Y. Huang, F. Liu, Y. Zhao, L. Cao and J. Ge, *Science*, 2020, **368**, 779.

50 W. Hao, J. A. Wojdyla, R. Zhao, R. Han, R. Das, I. Zlatev, M. Manoharan, M. Wang and S. Cui, *PLoS Pathog.*, 2017, **13**, e1006474.

51 R. N. Kirchdoerfer and A. B. Ward, *Nat. Commun.*, 2019, **10**, 2342.

52 M. Ahmad, A. Dwivedy, R. Mariadasse, S. Tiwari, J. Jeyakanthan and B. K. Biswal, *ACS Omega*, 2020, DOI: 10.31219/osf.io/fjnzc.

53 M. Yazdanian, S. L. Glynn, J. L. Wright and A. Hawi, *Pharm. Res.*, 1998, **15**, 1490.